

## Structure of proton drip-line nuclei around doubly magic $^{48}\text{Ni}$

W. Nazarewicz,<sup>1,2,3</sup> J. Dobaczewski,<sup>3,4</sup> T. R. Werner,<sup>3,4</sup> J. A. Maruhn,<sup>4,5</sup> P.-G. Reinhard,<sup>4,6</sup> K. Rutz,<sup>5</sup> C. R. Chinn,<sup>7</sup>  
A. S. Umar,<sup>7</sup> and M. R. Strayer<sup>2</sup>

<sup>1</sup>*Department of Physics, University of Tennessee, Knoxville, Tennessee 37996*

<sup>2</sup>*Physics Division, Oak Ridge National Laboratory, P.O. Box 2008, Oak Ridge, Tennessee 37831*

<sup>3</sup>*Institute of Theoretical Physics, Warsaw University, Hoża 69, PL-00681, Warsaw, Poland*

<sup>4</sup>*Joint Institute for Heavy Ion Research, Oak Ridge National Laboratory, P.O. Box 2008, Oak Ridge, Tennessee 37831*

<sup>5</sup>*Institut für Theoretische Physik, Universität Frankfurt, D-60325 Frankfurt, Germany*

<sup>6</sup>*Institut für Theoretische Physik, Universität Erlangen, Staudtstr. 7, D-91058 Erlangen, Germany*

<sup>7</sup>*Department of Physics, Vanderbilt University, Nashville, Tennessee 37235*

(Received 23 August 1995)

Properties of proton-rich nuclei around doubly magic  $^{48}_{28}\text{Ni}_{20}$  are studied in the framework of the self-consistent mean-field theory (Hartree-Fock, Hartree-Fock-Bogoliubov, and relativistic mean field). Various effective interactions are employed to investigate two-proton separation energies, deformations, single-particle levels, proton average potentials, and diproton partial decay half-lives in this mass region.

PACS number(s): 21.10.-k, 21.30.Fe, 21.60.Jz, 27.40.+z

### I. INTRODUCTION

The structure of exotic nuclei, i.e., nuclei with extreme isospin values, is one of the most exciting challenges in low-energy nuclear physics today. On the proton-rich side of the periodic table, the proton drip line has been delineated up to  $Z=83$  [1]. In several cases, it has been possible to go beyond the line of proton stability. Due to their long lifetimes, ranging from  $10^{-6}$  s to a few seconds [2], proton-unstable nuclei (proton emitters) are unique laboratories to study properties of single-proton orbitals, details of the proton mean field in the surface region, and residual correlations. Experimental and theoretical investigations of proton emitters promise to open up a wealth of new physics associated with the residual interaction coupling between bound states and extremely narrow resonances in the region of very low density of single-particle levels.

On the neutron-rich side, the drip line has been approached only for very light nuclei [3]. In contrast to proton-rich systems, which are stabilized by the Coulomb barrier, nuclei close to the neutron drip line are very weakly bound and, consequently, they are very extended spatially. Hence, the influence of the particle continuum is very important.

Because of the presence of collective modes and intruder states, the *sd*f nuclei, i.e., those with  $10 \leq N$ ,  $Z \leq 26$ , form an interesting playground to confront the large-scale spherical shell model with the approaches based on the mean-field theory. Indeed, nuclei from this region are heavy enough to exhibit low-energy collective phenomena and, at the same time, they are sufficiently light to be treated by the state-of-the-art shell-model techniques [4–6]. On the other hand, both approaches use different input and have rather different scopes.

The shell model is strongly based on the experimental data in a given restricted region of the nuclear chart. It uses the single-particle properties and two-body matrix elements, which are obtained by a best-fit procedure, and then are applied in the same region of nuclei, mainly to calculate the complete low-energy spectra. Of course it also gives the rela-

tive binding energies with respect to a given inert core. These binding energies, and hence also the separation energies, are very accurately reproduced (see Ref. [5], for example).

However, the shell-model results are difficult to extrapolate far from the experimentally explored regions, because their basic ingredients are unavailable there. For example, systematic changes in the single-particle spectra, when departing from the  $\beta$ -stability line, have to be known and/or modeled before the shell model is applied in the new region. Due to the scattering of nucleons from bound shell-model orbitals to unbound states the standard shell-model treatment seems inappropriate when applied to drip-line nuclei, and continuum states have to be taken into account explicitly. The resulting continuum shell model [7] properly takes into account decay channels; in the continuum shell model there are no effective one-body potentials, the interaction has a two-body character, and the single-particle energies are calculated self-consistently.

The mean-field approaches, which are applied in the present study, are based on global experimental data for nuclei throughout the nuclear chart. Their principal goal is to obtain a fair description of bulk properties of nuclei (masses, radii), mostly for the ground states only. In restricted regions of nuclei the mean-field approaches cannot compete for precision with the shell model. On the other hand, for quantities which involve the spatial dimensions, such as the radii, Coulomb energies, tunneling probabilities, etc., and for weakly bound systems where the particle continuum effects cannot be ignored, the mean-field theory has certain advantages. Therefore, in many respects, the shell-model and mean-field calculations are complementary.

The mean-field methods may better take into account large-scale changes of structure of nuclei far from stability. For such predictions one needs the best possible effective interactions. The main objective of our study is, therefore, to investigate the self-consistent mean-field theories with various interactions, and compare the results to experimental data and shell-model analyses. This is done for proton-rich nuclei around the doubly magic  $^{48}\text{Ni}$ . The degree of agree-

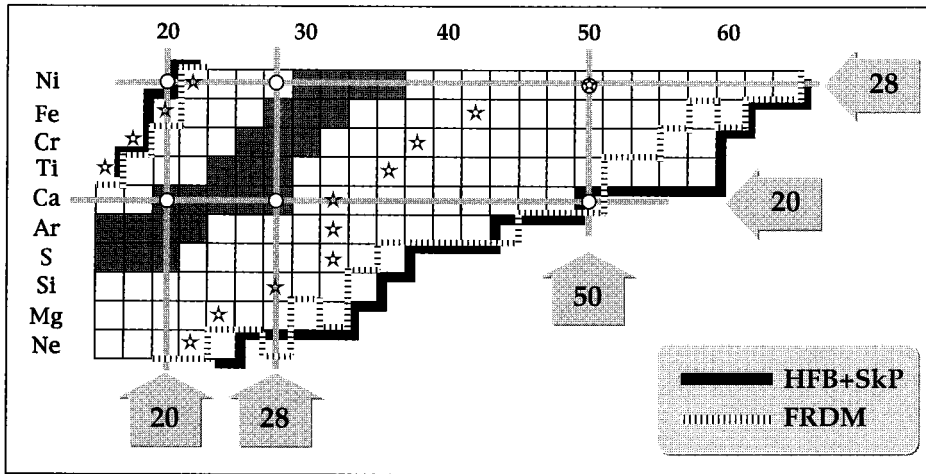


FIG. 1. Part of the chart of the nuclides corresponding to the region of nuclei with  $N \geq 18$  and  $10 \leq Z \leq 28$  (only even-even systems are presented). The lightest and heaviest isotopes known experimentally are indicated by the stars. The two-particle drip lines calculated with the spherical HFB+SkP model [23,56,44] and with the macroscopic-microscopic FRDM [25] are indicated by means of thick black and broken lines, respectively. See text for more details.

ment with the modern shell-model calculations in the region where (i) the configuration space is not prohibiting and (ii) the effect of the particle continuum is less severe due to the Coulomb barrier gives us more confidence in extrapolating the mean-field results to more exotic systems on the neutron-rich side, where, due to extremely large configuration spaces and continuum effects, the standard nuclear shell model cannot be used.

The paper is organized as follows. Section II discusses the borders of this region (i.e., the particle drip lines). The models employed are described in Sec. III. Sections IV and V contain the analysis of binding energies, deformations, and separation energies of  $N=18, 20$ , and  $22$  isotones. Coulomb energy displacements and single-particle energies around  $^{48}\text{Ni}$  are calculated in Sec. VI and the diproton lifetimes are estimated in Sec. VII. Finally, conclusions are contained in Sec. VIII.

## II. THE PERIODIC CHART OF THE *sd*f NUCLEI

Figure 1 displays the experimental situation in the *sd*f region of nuclei with  $N \geq 16$  and  $10 \leq Z \leq 28$  (only even-even systems are presented). The lightest and heaviest isotopes known experimentally are indicated by the stars. According to a recent experimental study [8] based on the fragmentation of  $^{58}\text{Ni}$  (see also the earlier Refs. [9,10]), the nuclei  $^{38}\text{Ti}$ ,  $^{46}\text{Fe}$ , and  $^{50}\text{Ni}$  are particle stable. On the neutron-rich side, the heaviest even-even isotopes found experimentally in this region are  $^{32}\text{Ne}$  [11],  $^{36}\text{Mg}$  [12],  $^{42}\text{Si}$  [13],  $^{48}\text{S}$  [13],  $^{50}\text{Ar}$  [12],  $^{52}\text{Ca}$  [14],  $^{58}\text{Ti}$  [15],  $^{62}\text{Cr}$  [14],  $^{68}\text{Fe}$  [16], and  $^{78}\text{Ni}$  [17].

In the region of the periodic chart shown in Fig. 1, there are six doubly magic nuclei, i.e., the Ca and Ni isotopes with  $N=20, 28$ , and  $50$ . Three of them, namely,  $^{40}\text{Ca}$ ,  $^{48}\text{Ca}$ , and  $^{56}\text{Ni}$ , are well known experimentally. Very recently, three events attributed to  $^{78}\text{Ni}$  have been reported [17]. This very neutron-rich nucleus, which has recently attracted considerable interest [18–21], is expected to lie a fair distance from the neutron drip line (see Fig. 1). The remaining two doubly magic nuclei are drip-line systems. The very proton-rich nucleus  $^{48}\text{Ni}$  is expected to lie on the edge of proton stability [22]. The neutron stability of  $^{70}\text{Ca}$  still remains an open question (see the discussion below).

The theoretical two-proton and two-neutron drip lines cal-

culated with the spherical Hartree-Fock-Bogoliubov (HFB) model with the effective Skyrme interaction SkP [23,24] and with the macroscopic-microscopic finite-range droplet model (FRDM) [25] are indicated in Fig. 1 by thick black and broken lines, respectively. The calculated two-proton drip lines are rather similar in both models. In particular, the doubly magic  $^{48}\text{Ni}$  is predicted to be two-proton unstable while its lighter isotope  $^{46}\text{Fe}$  is expected to be very weakly bound in the HFB+SkP model. (In the FRDM calculations, this nucleus has a two-proton separation energy very close to zero; see the discussion in Sec. V.)

As far as the neutron drip line is concerned, there are clear differences between the model predictions. The largest disagreement is seen for the Ti isotopes, where the two-neutron drip lines calculated in the FRD and HFB+SkP models differ by eight neutron numbers. An interesting effect is seen in the FRDM calculations for Ne, Mg, and Fe isotopes, where there appear local islands of particle stability *beyond* the two-neutron drip line (e.g., the nucleus  $^{38}\text{Ne}$  is two-neutron stable, while  $^{34,36}\text{Ne}$  are not). As discussed in Ref. [26], such a situation might be caused by configuration/shape changes. A spectacular example, due to the transition from spherical to deformed shapes, is the backbending in the  $S_{2n}$ -vs- $N$  plot for the Sm isotopes seen at  $N \sim 88$  [26]. (The effect of deformation is not considered in the HFB+SkP calculations, which yield a single-valued dependence of  $S_{2n}$  on  $N$ .)

As a typical example of the theoretical uncertainty when extrapolating very far from the line of  $\beta$  stability, Table I displays the values of the two-neutron separation energy for  $^{70}\text{Ca}$  predicted with the Hartree-Fock (HF), relativistic mean field (RMF), and HFB models with different effective interactions (see Sec. III for details). In the HF and RMF calculations performed here, pairing correlations are treated by means of the constant-gap approximation with the pairing gaps taken from the HFB+SkP model (see Sec. III). Except for the RMF+L1 and RMF+TS models of Ref. [27], which predict unusually strong neutron binding, calculations suggest that  $^{70}\text{Ca}$  is very close to the neutron drip line; namely, according to HF+SIII, HF+SkI6, HF+SLy4, HFB+SkP, and HFB+SIII $^{\delta p}$ , the nucleus  $^{70}\text{Ca}$  lies very close to (but beyond) the two-neutron drip line, while according to HF+SkM\*, HF+SkI1, RMF+NL-SH, RMF+PL40, and

TABLE I. Predicted values of  $S_{2n}$  for  ${}^{70}_{20}\text{Ca}_{50}$ . In the HF, RMF+NL-SH, and RMF+PL40 calculations, pairing correlations are treated by means of the constant-gap approximation with the values of pairing gaps taken from the HFB+SkP calculations [ $\Delta_p=0$ ,  $\Delta_n({}^{68}\text{Ca})=1.37$  MeV,  $\Delta_n({}^{70}\text{Ca})=1.32$  MeV].

Model	$S_{2n}$ (MeV)	Model	$S_{2n}$ (MeV)
HF+SIII	-0.18	RMF+L1 <sup>a</sup>	20.78
HF+SkM*	1.33	RMF+TS <sup>a</sup>	7.35
HF+SkI6	-1.85	RMF+NL-SH	0.60
HF+SLy4	-1.48	RMF+PL40	1.00
HF+SkI1	1.31	FRDM <sup>b</sup>	0.39
HFB+SkP	-0.24	HFB+SIII <sup><math>\delta\rho</math></sup>	-0.02

<sup>a</sup>From Reference [27].

<sup>b</sup>From Reference [25].

FRDM, this nucleus is (very weakly) bound. Considering the rather small theoretical values of  $|S_{2n}|$ , the question of particle stability of this extremely exotic, doubly magic system remains open. Experimentally, the direct study of  ${}^{70}\text{Ca}$  is impossible at present because this system is far too neutron rich. One can hope, however, that some indirect information on  ${}^{70}\text{Ca}$  will become available from the analysis of solar-system  $r$ -process abundance distributions [28].

In the present work, we concentrate on properties of another exotic doubly magic nucleus,  ${}^{48}_{28}\text{Ni}_{20}$ , and its neighbors. As mentioned above, the proton-rich nuclei from the  $1f_{7/2}$  region have recently been subjects of several studies based on the intermediate-energy heavy-ion fragmentation technique [8–10,29]. As discussed in Refs. [4,30,6], the region around  ${}^{48}\text{Ni}$  is a very promising one in which to look for diproton decay, the best candidates being  ${}^{38}\text{Ti}$ ,  ${}^{45}\text{Fe}$ , and  ${}^{48}\text{Ni}$ .

The experimental information on the very proton-rich  $sd$ f systems is very scarce. The masses and, consequently, the two-proton separation energies  $S_{2p}$  are not known. In some cases, the binding energies of the  $T_3 < 0$  nuclei [ $T_3 = (N-Z)/2$ ] can be deduced from a quadratic isobaric multiplet mass equation (IMME) [31]:

$$B(A, T, T_3) = a(A, T) + b(A, T)T_3 + c(A, T)T_3^2. \quad (1)$$

The coefficients  $a$ ,  $b$ , and  $c$  of the IMME can be either determined experimentally from known masses [32–35] or calculated perturbatively using the isospin-nonconserving interaction [36]. In particular, the relation (1) can be applied to determine the binding energy difference between mirror nuclei with  $T_3 = \pm T$ :

$$B(A, T, T_3 = -T) = B(A, T, T_3 = T) - 2b(A, T)T. \quad (2)$$

This method has proven to be a very accurate tool for predicting binding energies of proton-rich nuclei [4,6]. It is worth noting that shell-model techniques in general and the IMME in particular do not take into account variations in the Coulomb energy of drip-line nuclei due to weak binding. As estimated by the self-consistent theory (see Sec. VI), the contribution to the Coulomb energy shift caused by an increased Coulomb radius can be as large as a few hundred keV.

### III. THE MODELS

In this study, several self-consistent models based on the HF+BCS, HFB, and RMF approaches are used. In the following, their effective interactions and other parameters are discussed briefly.

The spherical HFB-Skyrme calculations have been carried out in spatial coordinates following the method introduced in Ref. [23]. Several effective interactions are employed. These are (i) the Skyrme parametrization SkP introduced in Ref. [23] (SkP has exactly the same form in the particle-hole ( $p$ - $h$ ) and pairing channels); (ii) the Skyrme interaction SkP <sup>$\delta\rho$</sup>  of Ref. [37] (which in the  $p$ - $h$  channel is the SkP Skyrme parametrization, while its pairing component is given by the density-dependent  $\delta$  interaction (DDDI) [38–40],

$$V^{\delta\rho}(\mathbf{r}, \mathbf{r}') = \left( V_0 + \frac{1}{6} V_3 \rho^\gamma \right) \delta(\mathbf{r} - \mathbf{r}'), \quad (3)$$

where  $\rho = \rho(\mathbf{r})$  is the isoscalar nucleonic density; (iii) the force SIII <sup>$\delta\rho$</sup>  (in the  $p$ - $h$  channel, this is the SIII Skyrme parametrization [41]; its pairing part is given by the DDDI of Ref. [37]); (iv) the force SkM <sup>$\delta\rho$</sup>  (in the  $p$ - $h$  channel, this is the SkM\* Skyrme parametrization [42] and its pairing part is given by the DDDI with the parameters of Ref. [37]).

All HFB-Skyrme results have been obtained using a box of 20 fm. All other details of the calculations, in particular the determination of the pairing phase space, closely follow the method outlined in Ref. [23].

The pairing fields generated by the density-dependent pairing interaction, such as SkP or DDDI, are surface peaked and give rise to a strong coupling to the particle continuum [43,39,44]. Figure 2 illustrates this effect for the  $N=20$  isotones  ${}^{30}\text{Ne}$  (neutron rich) and  ${}^{46}\text{Fe}$  (proton rich). The single-particle densities calculated in the HFB+SkP model are shown in the upper portion. In  ${}^{30}\text{Ne}$ , the neutron skin (i.e., an excess of neutrons at large distances) is clearly seen. Although both nuclei have the same number of neutrons, their neutron distributions are quite different. This can be explained in terms of the strong coupling between neutron and proton systems, which gives rise to a larger neutron density in  ${}^{46}\text{Fe}$  in the surface region. However, at still larger distances ( $r > 5.2$  fm), the neutron density in  ${}^{30}\text{Ne}$  exceeds that in  ${}^{46}\text{Fe}$ , due to a weaker neutron binding. Because of an excess of protons, in  ${}^{46}\text{Fe}$  the proton density is larger than the neutron density, which is particularly pronounced at large distances (proton skin).

The corresponding pairing densities  $\tilde{\rho}$  are displayed in the bottom portion of Fig. 2. (The pairing density is defined as in Refs. [23,44],  $\tilde{\rho}(r) = \sum_{\mu} u_{\mu} v_{\mu} |\tilde{\psi}_{\mu}(r)|^2$ , where  $\mu$  label the canonical states.) Several observations are noteworthy. First, neutron pairing is different from zero in both nuclei in spite of their magic neutron number  $N=20$  [24]. Secondly,  $\tilde{\rho}$  becomes very extended spatially with reduced binding. Indeed, the neutron pairing density in  ${}^{30}\text{Ne}$  and the proton pairing density in  ${}^{46}\text{Fe}$  disappear rather slowly at large distances. Thirdly, the pairing densities are peaked in the surface region. (For more discussion of pairing effects in drip-line nuclei, we refer the reader to Ref. [44].)

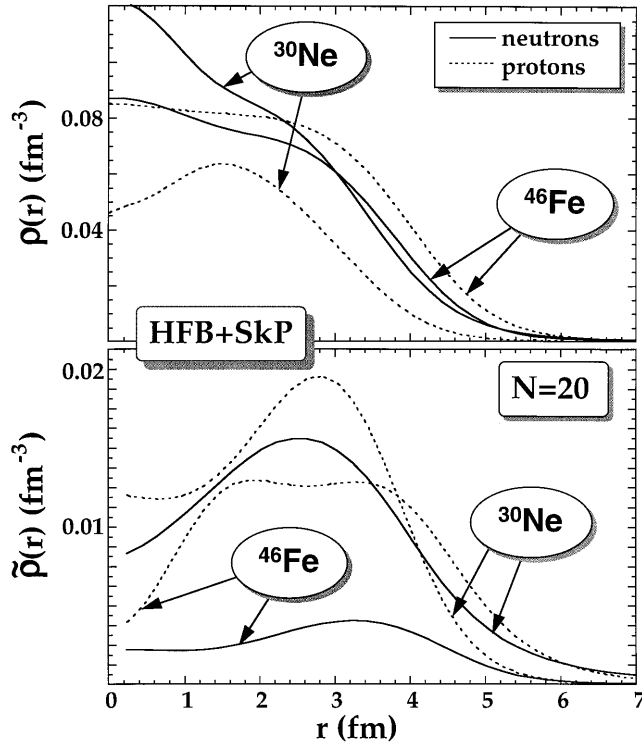


FIG. 2. Top: Single-particle densities  $\rho(r)$  for  $^{30}\text{Ne}$  and  $^{46}\text{Fe}$  calculated in the HFB+SkP model. Bottom: Corresponding pairing densities  $\tilde{\rho}(r)$  defined as in Refs. [23,44].

A set of spherical HFB calculations has also been performed using the finite-range Gogny interaction D1S of Ref. [45]. The pairing field is calculated from the D1S force, thus producing a consistent microscopic description for both the mean field and the pairing interaction. As discussed in Ref. [44], the D1S interaction produces pairing densities that have volume character (the pairing component of D1S is density independent). The parameters of the D1S interaction were chosen to reproduce certain global properties of a set of spherical nuclei and of nuclear matter [46,47]. The HFB+Gogny results presented here were obtained by expanding the HFB wave functions in a harmonic oscillator basis containing 18 shells.

The HF+BCS calculations were performed using the techniques of Ref. [48] with several Skyrme parametrizations: SIII, SkM\*, SkI1 [49], SLy4 [50], and SkI6. The last force, SkI6, is a variant of SkI1 which was refitted with the basis data set of Ref. [49] and additional particular emphasis on energy differences along isotopic chains ( $^{40}\text{Ca}$ – $^{48}\text{Ca}$  and the isotopes of Sn) aiming at a more reliable extrapolation towards the drip line. Apart from other parameters, these forces differ in their values of the effective mass for symmetric nuclear matter,  $m^*/m$ . For most of the interactions employed in this study, the effective mass is significantly lower than 1; namely,  $m^*/m=0.69, 0.69, 0.76,$  and  $0.79$  for SkI6, SLy4, SIII, and SkM\*, respectively. The only exception is SkP which has  $m^*/m=1$ .

In the RMF+BCS calculations, two parametrizations have been used: NL-SH [51] and PL40 [52]. These models yield rather low values for the effective mass:  $m^*/m=0.58$  (PL40) and  $0.66$  (NL-SH). Note that we are using the param-

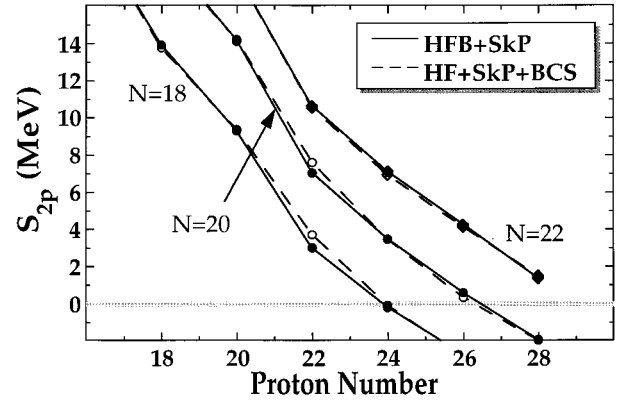


FIG. 3. Two-proton separation energies for the even-even  $N=18, 20,$  and  $22$  isotones predicted in the HFB and HF+BCS calculations with the SkP effective interaction.

etrization PL40 which employs a stabilized form of the functional for the scalar field. The more standard parametrization NL1 from [53] is likely to fail under exotic conditions due to instability of the scalar field at high densities.

It is well known [23,37,44,54] that traditional models of pairing correlations (BCS) become inappropriate when approaching particle drip lines. The main drawback is the scattering of nucleons from bound shell-model orbitals to unbound states, giving rise to an unphysical component in the nucleonic density with the wrong asymptotic behavior. This problem becomes particularly severe for neutron-rich nuclei where the particle continuum lies very low in energy. On the proton-rich side, the effect of the continuum is weaker [55] because of the Coulomb barrier which tends to localize the proton density in the nuclear interior.

The proper mean-field tool to describe the pairing in weakly bound nuclei is the HFB theory. In particular, the use of the HFB formalism guarantees the correct asymptotic behavior of nucleonic densities [23,44]. Consequently, this method is free from the problem of an artificial “particle gas” inherent to the HF+BCS approximation. Interestingly, relative binding energies (e.g., separation energies) seem to be less sensitive to the particle-gas problem, provided the self-consistent pairing gaps obtained from the HFB calculations are used in HF+BCS within the fixed-gap approximation (the HF+BCS4 method of Ref. [23]). In order to illustrate this point, Fig. 3 displays theoretical two-proton separation energies  $S_{2p}$  for the even-even  $N=18, 20,$  and  $22$  isotones obtained in the HFB and HF+BCS calculations with the SkP effective interaction. The values of HFB pairing gaps used in HF+BCS are displayed in Table II. From Fig. 3 it is seen that the values of  $S_{2p}$  obtained in the HFB and HF+BCS calculations are very similar. Guided by these results, in the HF+BCS and RMF+BCS calculations performed in this study, we always use the same constant values of the pairing gaps listed in Table II. However, it has to be emphasized that the excellent agreement between HFB and HF+BCS for the separation energies illustrated in Fig. 3 does not extend to other quantities such as radii [23,54,56], where the effect of the positive-energy quasibound states is dramatic.

TABLE II. Self-consistent average values of the neutron and proton pairing gaps,  $\Delta_n$  and  $\Delta_p$ , (in MeV) for  $N=18, 20$ , and  $22$  even-even isotones calculated with the HFB+SkP model.

$Z$	$N=18$		$N=20$		$N=22$	
	$\Delta_n$	$\Delta_p$	$\Delta_n$	$\Delta_p$	$\Delta_n$	$\Delta_p$
8	1.81	0.02	1.78	0.02	1.80	0.02
10	1.59	1.71	1.50	1.75	1.76	1.70
12	1.40	1.67	1.29	1.65	1.59	1.66
14	1.26	1.02	1.18	1.06	1.45	1.05
16	1.31	0.77	1.21	1.04	1.52	1.14
18	1.43	1.12	1.17	1.20	1.65	1.27
20	1.38	0.40	0.51	0.29	1.50	0.53
22	1.29	1.22	0.37	1.29	1.39	1.23
24	1.22	1.29	0.34	1.34	1.30	1.31
26	1.22	1.18	0.32	1.13	1.28	1.17
28	1.18	0.99	0.43	0.81	1.27	0.82

#### IV. EQUILIBRIUM DEFORMATIONS

Most calculations presented in this study assume spherical shapes which is fairly well justified for the proton-rich  $N=18, 20$ , and  $22$  isotones. Indeed, according to the FRDM calculations [25], all even-even nuclei with  $N=18, 20$ , and  $22$  and  $14 \leq Z \leq 28$  are spherical. In the extended Thomas-Fermi with Strutinski-integral (ETFSI) model calculations [57], the  $N=20$  isotones and the  $Z=20$  and  $28$  isotopes are practically spherical. (Only  $^{46}\text{Fe}$  and  $^{50}\text{Ni}$  are predicted to be slightly deformed,  $\beta_2=0.14$ ; the associated deformation energy  $E_{\text{def}}$  is about 0.2 MeV.) The largest deformations are calculated in ETFSI for  $^{42}\text{Cr}_{18}$  ( $\beta_2=0.24$ ,  $E_{\text{def}}=1.26$  MeV) and  $^{46}\text{Cr}_{22}$  ( $\beta_2=0.24$ ,  $E_{\text{def}}=1.20$  MeV); the contribution to  $S_{2p}$  due to deformation does not exceed 900 keV in these isotopes.

The potential energy curves for the proton-rich  $N=18, 20$ , and  $22$  isotones are shown in Figs. 4 (HF+SIII) and 5 (RMF+PL40) as functions of the mass quadrupole moment. In general, deformation effects are predicted to be weak. The tendency towards deformation is slightly stronger in RMF

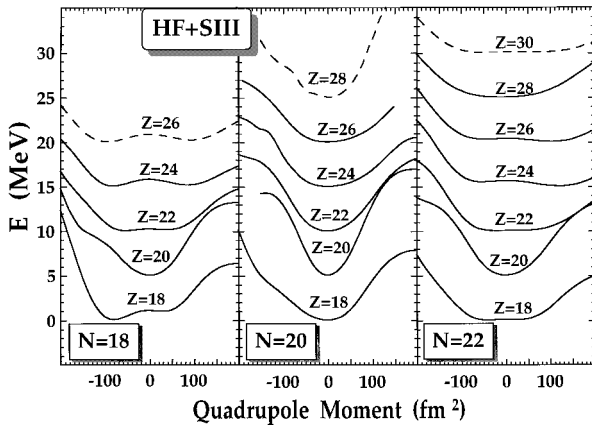


FIG. 4. Potential energy curves versus total quadrupole moment for proton-rich even-even  $N=18, 20$ , and  $22$  isotones calculated in the HF+BCS+SIII model. The isotopes that are predicted to be unbound ( $\lambda_p > 0$ ) are indicated by dashed lines.

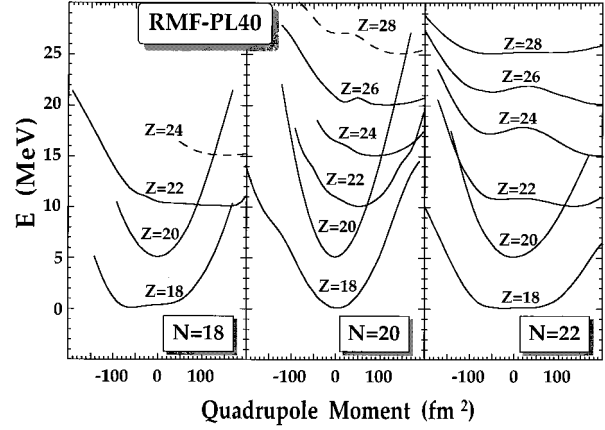


FIG. 5. Same as Fig. 4 except for the RMF+BCS+PL40 model.

+PL40 calculations, especially for the  $N=22$  isotones of Cr and Fe. The largest differences between HF+SIII and RMF+PL40 are seen for weakly bound or slightly unbound nuclei such as  $^{48}\text{Ni}$ . Here, the self-consistent results are not stable due to the occupation of positive-energy quasibound proton states.

In order to illustrate the effect of quasibound states on the HF+BCS results, Fig. 6 shows the HF+BCS+SIII potential energy curve of  $^{50}\text{Ni}$ , together with the total occupation of positive-energy states,

$$n_p(\varepsilon_p > 0) = \sum_{i, \varepsilon_i > 0} 2v_i^2, \quad (4)$$

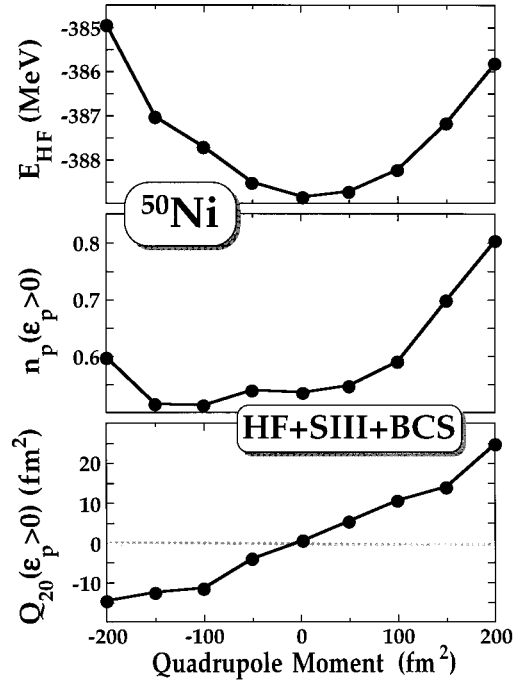


FIG. 6. Top: Potential energy curve of  $^{50}\text{Ni}$  versus the total quadrupole moment calculated in the HF+BCS+SIII' model. Middle: The total occupation of the positive-energy states. Bottom: The contribution of the positive-energy states to the total quadrupole moment.

and the contribution of the positive-energy states to the total quadrupole moment,

$$Q_{20}(\varepsilon_p > 0) = \sum_{i, \varepsilon_i > 0} 2v_i^2 q_{20,i}. \quad (5)$$

In Eqs. (4) and (5),  $v_i^2$  and  $q_{20,i}$  are the BCS occupation coefficient and the single-particle quadrupole moment, respectively. The calculations presented in Fig. 6 were performed by discretizing the energy functional on a three-dimensional Cartesian spline collocation lattice of size  $(20 \text{ fm})^3$ , without imposing any self-consistent symmetry [58]. In the following, we shall refer to this model as HF+BCS+SIII'. The small differences between the HF+BCS+SIII and HF+BCS+SIII' results (cf. the potential energy curves of Figs. 4 and 6) can be attributed to (i) a small triaxiality which appears in the HF+BCS+SIII' model (the  $Q_{20}$  moment was constrained but  $Q_{22}$  was not) and (ii) the different description of quasibound states in the two approaches. In the considered deformation range, the occupation of quasibound proton states due to BCS pairing varies between 0.5 and 0.8, which is less than 2% of the total number of particles in  $^{50}\text{Ni}$ . At the same time, however, the contribution from unbound states to  $Q_{20}$  is large, about 10%. By inspecting single-particle contributions to  $Q_{20}(\varepsilon_p > 0)$ , one finds that its significant part comes from the states with  $\varepsilon_i > 5 \text{ MeV}$  having very low values of  $\langle j_z \rangle$  ( $\hat{j}_z$  is not conserved in the calculations), small occupations, and very large values of  $q_{20,i}$  ranging between 30 and 70  $\text{fm}^2$ . The wave functions of these states are not localized inside the nuclear volume, but they are pushed towards large values of  $z^2$  by the constraining quadrupole field. These spurious states, resulting from the discretization of the particle continuum, also give rise to the large proton hexadecapole moment, which is 10–20 times larger than the neutron hexadecapole moment. As discussed in Ref. [59], the nonlocalized quasibound states are often degenerate, reflecting the fact that they are not affected by the spin-dependent part of the interaction. The above result indicates that, due to non-negligible couplings to the nonphysical continuum states, the constrained HF+BCS approach becomes rather unreliable when applied to nuclei close to the particle drip lines.

## V. SEPARATION ENERGIES

Figures 7–9 display the two-proton separation energies  $S_{2p}$  for the even-even  $N=18, 20,$  and  $22$  isotones calculated in this study. In addition, the results for the proton drip-line isotopes of Cr, Fe, and Ni are shown in Table III and compared with predictions of the FRDM [25] and ETFSI [57] and the analysis based on the IMME [4,6,32]. Experimental data (or  $S_{2p}$  values deduced from systematic trends) taken from Audi and Wapstra [60] are also shown.

Apart from calculations based on the SkM\* Skyrme parametrization, which tends to overbind all nuclei discussed (cf. Ref. [37] for comparison between SkP, SIII, and SkM\*), all models predict  $^{48}\text{Ni}$  to be two-proton unstable and  $^{50}\text{Ni}$  to be bound. The nucleus  $^{46}\text{Fe}$  is expected to be bound in all models (FRDM gives  $S_{2p}$  very close to zero), as well as  $^{44}\text{Cr}$ . Another borderline nucleus in this region,  $^{42}\text{Cr}$ , is predicted to be two-proton unstable by all models

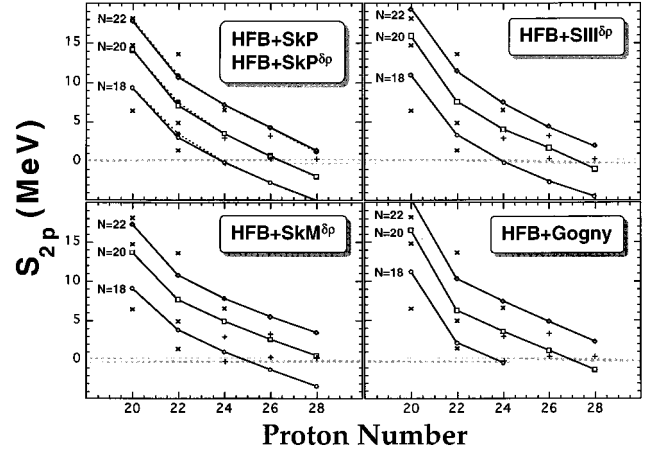


FIG. 7. Two-proton separation energies for the even-even  $N=18, 20,$  and  $22$  isotones with  $20 \leq Z \leq 28$  predicted in the HFB calculations. The SkP  $^{\delta p}$  results are indicated by a dotted line in the upper left panel. The experimental data from Ref. [60] are marked by “x” symbols or, if deduced from systematic trends, by “+.”

except ETFSI, SIII, and SkM\*.

The influence of deformation on  $S_{2p}$  is illustrated in Figs. 8 (HF+SIII) and 9 (RMF+PL40). In the HF+SIII model, the difference between spherical and deformed calculations is small. In the RMF+PL40 calculations, the strongest effect is predicted for the  $N=22$  isotones, especially  $^{46}\text{Cr}$  and  $^{50}\text{Ni}$ . In neither case does the inclusion of deformation seem to influence the predicted position of the two-proton drip line.

Most models give a rather good agreement with the data for the  $N=20$  isotones except  $^{42}\text{Ti}$  which is reproduced only in the RMF calculations. All models strongly underbind  $^{44}\text{Ti}$  and strongly overbind  $^{38}\text{Ca}$ .

## VI. SINGLE-PARTICLE ENERGIES AROUND $^{48}\text{Ni}$

Valuable information about properties of an unknown nucleus ( $N, Z$ ) can be obtained from studies of its known mirror partner ( $N'=Z, Z'=N$ ). In particular, there exists a

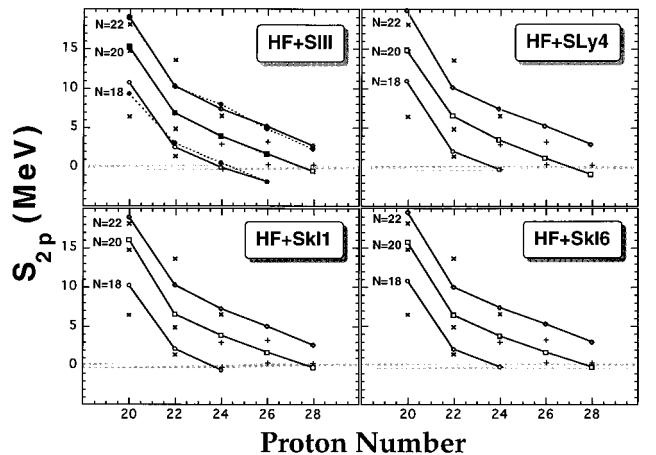


FIG. 8. Same as Fig. 7 except for the HF+BCS calculations. The deformed SIII calculations are indicated by a dotted line in the upper left panel.

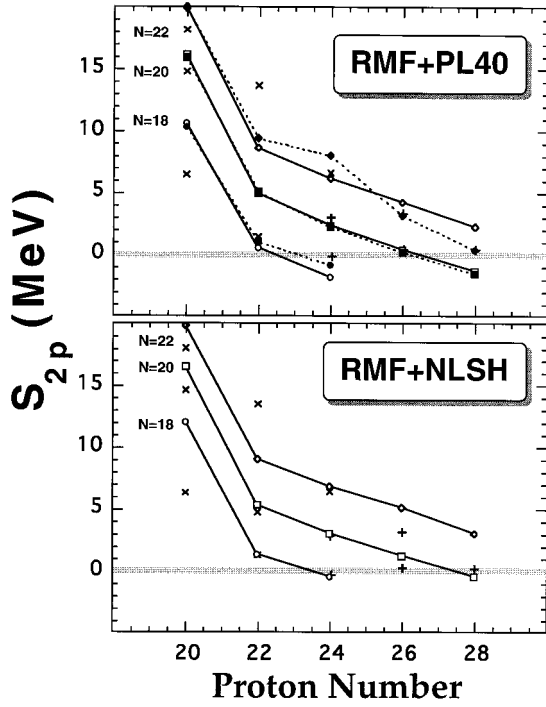


FIG. 9. Same as Fig. 7 except for the RMF+BCS calculations. The deformed PL40 calculations are indicated by a dotted line in the upper panel.

correspondence between excited levels of two mirror nuclei; the relative energy shift can be explained by the Coulomb energy difference (including the isospin-nonconserving nuclear interactions and other electromagnetic corrections) [61,62]. There exist many phenomenological expressions that relate neutron and proton energies in mirror nuclei. For instance, Goldansky [22] proposed a simple expression for the difference between proton,  $e_p$ , and neutron,  $e_n$ , single-particle energies:

$$\begin{aligned} \Delta^\pm e &\equiv e_p({}^A_Z M_N) - e_n({}^A_N M_Z) \\ &\approx 1.2 \left\{ \frac{Z-1}{A^{1/3}} - \frac{1}{2}(Z-N-1) \right. \\ &\quad \left. \times (A-2) \left[ \frac{1}{(A-1)^{1/3}} - \frac{1}{A^{1/3}} \right] \right\} \text{ MeV,} \end{aligned} \quad (6)$$

where the sign in the superscript denotes the sign of  $N-Z$ . Relations such as (6) have a global character, i.e., they do not take into account the microscopic structure of individual single-particle orbitals (e.g., angular momentum or radial features of the wave function). Therefore, in the following, we calculate  $\Delta^\pm e$  self-consistently for each single-particle orbital of interest.

The mirror nucleus to  ${}^{48}\text{Ni}$  is the well-known  $T_3=4$  system,  ${}^{48}\text{Ca}$ . Figure 10 (bottom) shows the energy displacements,

$$\Delta^- e_i \equiv e_{ip}({}^{48}\text{Ni}) - e_{in}({}^{48}\text{Ca}), \quad i \equiv (n\ell j), \quad (7)$$

between the proton single-particle energies in  ${}^{48}\text{Ni}$  and the neutron single-particle energies in  ${}^{48}\text{Ca}$ , versus the proton

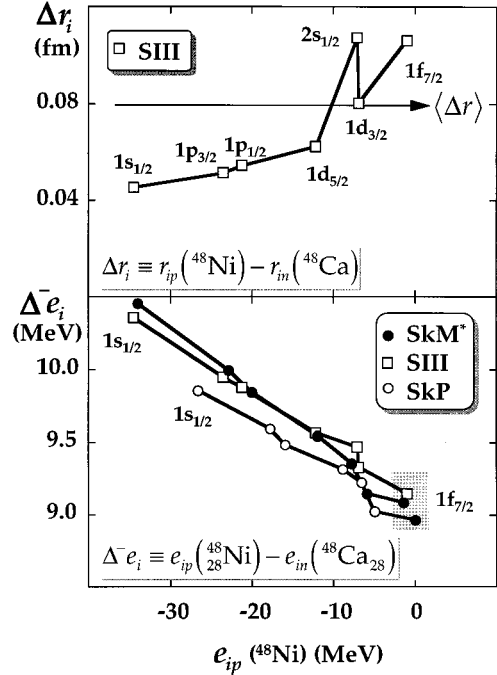


FIG. 10. Bottom: Difference  $\Delta^- e_i [i \equiv (n\ell j)]$  between the proton single-particle energies in  ${}^{48}\text{Ni}$  and the neutron single-particle energies in  ${}^{48}\text{Ca}$ , calculated in the HF+SkM\*, HF+SkP, and HF+SIII models. Top: Difference  $\Delta r_i$  between the rms radii of proton states in  ${}^{48}\text{Ni}$  and the rms radii of neutron states in  ${}^{48}\text{Ca}$ , calculated in the HF+SIII model. The average value  $\langle \Delta r \rangle \equiv \sqrt{\langle r_p^2 \rangle \times ({}^{48}\text{Ni}) - \sqrt{\langle r_n^2 \rangle \times ({}^{48}\text{Ca})}$  is indicated by the arrow.

single-particle energies in  ${}^{48}\text{Ni}$ , calculated in the HF+SkM\*, HF+SkP, and HF+SIII models. The single-particle energies predicted by the SkM\*, SkP, and SIII interactions are different. Although all three models yield rather similar spectra around the Fermi level, the single-particle spectrum of SkP is compressed relative to those of SkM\* and SIII, due to different effective masses [37]. However, in spite of the different single-particle spectra, the curves of  $\Delta^- e_i$  vs  $e_{ip}$  cluster in a rather narrow band (with the width of  $\sim 100$  keV) around the average value of  $\Delta^- e = -0.04e_p + 9$  MeV. (The weak dependence of  $\Delta^- e_i$  on properties of individual orbitals has already been observed in Ref. [63].) When applied to  ${}^{48}\text{Ni}$ , the simple expression (6) gives  $\Delta^- e = 8.54$  MeV.

From the experimental single-neutron energies in  ${}^{48}\text{Ca}$  and the energy correlation shown in Fig. 10, one can estimate the energies of the proton-hole orbitals in  ${}^{48}\text{Ni}$ :

$$e_{ip}({}^{48}\text{Ni}) = [9 \text{ MeV} + e_{in}({}^{48}\text{Ca})]/1.04 \quad (8)$$

(see Table IV). The deduced position of the  $e_{1f_{7/2}}$  shell is consistent with the value of the one-proton separation energy for  ${}^{48}\text{Ni}$  extracted in Ref. [4] from the IMME,  $S_p = 0.469$  MeV; in both cases the  $1f_{7/2}$  shell is predicted to be weakly bound.

A similar analysis can be performed for the neutron states in  ${}^{48}\text{Ni}$ . The difference  $\Delta^+ e_i$ ,

$$\Delta^+ e_i \equiv e_{ip}({}^{48}\text{Ca}) - e_{in}({}^{48}\text{Ni}), \quad i \equiv (n\ell j), \quad (9)$$

TABLE III. Experimental and predicted values of the two-proton separation energies  $S_{2p}$  for  $^{42,44}\text{Cr}$ ,  $^{46,48}\text{Fe}$ , and  $^{48,50}\text{Ni}$ . In the HF and RMF calculations, pairing was treated by means of the constant-gap approximation. In all cases, except the HF<sub>def</sub>+SIII and RMF<sub>def</sub>+PL40, calculations were performed at the spherical shape. For details see text.

Model	Ref. <sup>a</sup>	Ref. <sup>b</sup>	$S_{2p}$ (MeV)					
			$^{42}\text{Cr}_{18}$	$^{44}\text{Cr}_{20}$	$^{46}\text{Fe}_{20}$	$^{48}\text{Fe}_{22}$	$^{48}\text{Ni}_{20}$	$^{50}\text{Ni}_{22}$
Systematics	[60]		$-0.26 \pm 0.34$	$2.99 \pm 0.13$	$0.29 \pm 0.38$	$3.22 \pm 0.1$	$(-1.99) - (-0.97)^c$	$0.26 \pm 0.28$
Benenson	[32] <sup>d</sup>		-0.58	3.03	0.46	3.14	-1.33	0.54
Brown	[4] <sup>e</sup>		-0.50	2.90	0.45	3.14	-1.36	0.50
Ormand	[6] <sup>e</sup>		-0.45(15)	2.91(8)	0.34(15)	3.22(9)	-1.14(21)	
FRDM	[25]		-1.26	2.34	-0.06	4.04	-3.03	0.31
ETFSI	[57]		0.57	4.08	1.07	4.54	-1.76	1.07
HFB+SkP		[23]	-0.22	3.46	0.57	4.23	-1.97	1.33
HFB+SkP <sup><math>\delta p</math></sup>		[37]	-0.21	3.38	0.55	4.13	-2.10	1.08
HFB+SIII <sup><math>\delta p</math></sup>		[37]	-0.12	3.99	1.66	4.26	-1.04	1.84
HFB+SkM <sup><math>\delta p</math></sup>		[37]	0.96	4.81	2.53	5.39	0.44	3.41
HFB+Gogny		[46]	-0.45	3.52	1.07	4.79	-1.36	2.23
HF+SkM*		[42]	0.93	4.77	2.57	5.85	0.49	3.49
HF+SIII		[41]	0.01	4.00	1.73	5.24	-0.47	2.76
HF <sub>def</sub> +SIII		[41]	0.62	3.99	1.70	4.95	-0.47	2.36
HF+SkI1		[49]	-0.70	3.69	1.55	4.89	-0.38	2.48
HF+SkI6		[49]	-0.11	3.81	1.74	5.36	-0.14	3.07
HF+SLy4		[50]	-0.30	3.47	1.16	5.24	-0.93	2.88
RMF+PL40		[52]	-1.90	2.30	0.30	4.20	-1.40	2.20
RMF <sub>def</sub> +PL40		[52]	-0.89	2.18	0.12	3.12	-1.58	0.32
RMF+NL-SH		[51]	-0.50	3.00	1.20	5.10	-0.50	3.00

<sup>a</sup>Results taken from the reference indicated.

<sup>b</sup>Parameters taken from the reference indicated.

<sup>c</sup>From Ref. [9].

<sup>d</sup>From the IMME.

<sup>e</sup>From experimental binding energies of neutron-rich analogs with theoretical Coulomb energy shifts added.

between the proton single-particle energies in  $^{48}\text{Ca}$  and the neutron single-particle energies in  $^{48}\text{Ni}$  is shown in Fig. 11 (bottom) as a function of the neutron single-particle energies in  $^{48}\text{Ni}$ . The results of SkM\*, SkP, and SIII calculations are very similar: all values lie in a narrow band  $\Delta^+e = -0.006e_n + 6.7$  MeV between 6.6 and 7.2 MeV [for comparison, for  $^{48}\text{Ca}$ , Eq. (6) yields  $\Delta^+e = 6.76$  MeV]. This result, together with experimental single-proton energies in  $^{48}\text{Ca}$ , allows us to estimate the energies of single-neutron orbitals in  $^{48}\text{Ni}$ :

$$e_{in}({}^{48}\text{Ni}) = [e_{ip}({}^{48}\text{Ca}) - 6.7\text{MeV}] / 0.994, \quad (10)$$

see Table IV.

The different average behavior of  $\Delta^-e_i$  and  $\Delta^+e_i$  as a function of the single-particle energy can be explained in terms of the different radial behavior of the proton and neutron wave functions in  $^{48}\text{Ni}$  and  $^{48}\text{Ca}$ . Indeed, the Coulomb perturbation modifies the radial wave function of the proton in the analog state with respect to the corresponding neutron in the parent state (Thomas-Ehrman effect [64,65]), leading to a decrease in the energy difference between analog states. As discussed in detail in Ref. [62], the Thomas-Erhman effect is significant for loosely bound states (e.g., states in drip-line systems) and for states having low angular momentum.

The upper panels of Figs. 10 and 11 show the difference

$$\Delta r_i \equiv \langle r_p^2 \rangle_i^{1/2} - \langle r_n^2 \rangle_i^{1/2}, \quad i \equiv (n \ell j), \quad (11)$$

between the single-proton and single-neutron rms radii in the mirror nuclei  $^{48}\text{Ni}$  and  $^{48}\text{Ca}$  calculated in the HF+SIII model. The arrow indicates the average value  $\langle \Delta r \rangle \equiv \langle r_p^2 \rangle^{1/2} - \langle r_n^2 \rangle^{1/2}$ . While the single-proton radii in  $^{48}\text{Ca}$  are only slightly shifted ( $\sim 0.03$  fm) with respect to the single-neutron radii in  $^{48}\text{Ni}$  (Fig. 11), the proton radii in  $^{48}\text{Ni}$  are significantly larger than neutron radii in  $^{48}\text{Ca}$  ( $\sim 0.08$  fm), and the difference  $\Delta r_i$  has a pronounced dependence on the proton binding energy (Fig. 10). It is worth noting that for the low- $\ell$  states (such as  $2s_{1/2}$ ) and loosely

TABLE IV. Proton and neutron single-particle energies (in MeV) predicted in  $^{48}\text{Ni}$  from experimental data [66] in  $^{48}\text{Ca}$ . The uncertainties of the predicted values are tentatively deduced from the spread of theoretical results presented in Figs. 10 and 11.

Orbital	$^{48}\text{Ca}$		$^{48}\text{Ni}$	
	Experimental		Predicted	
	<i>n</i>	<i>p</i>	<i>n</i>	<i>p</i>
$2s_{1/2}$	-12.55	-15.3	$-22.1 \pm 0.2$	$-3.38 \pm 0.15$
$1d_{3/2}$	-12.52	-15.7	$-22.5 \pm 0.2$	$-3.41 \pm 0.15$
$1f_{7/2}$	-9.94	-9.6	$-16.4 \pm 0.1$	$-0.90 \pm 0.15$
$2p_{3/2}$		-1.9	$-8.7 \pm 0.1$	
$2p_{1/2}$		0.0	$-6.7 \pm 0.1$	

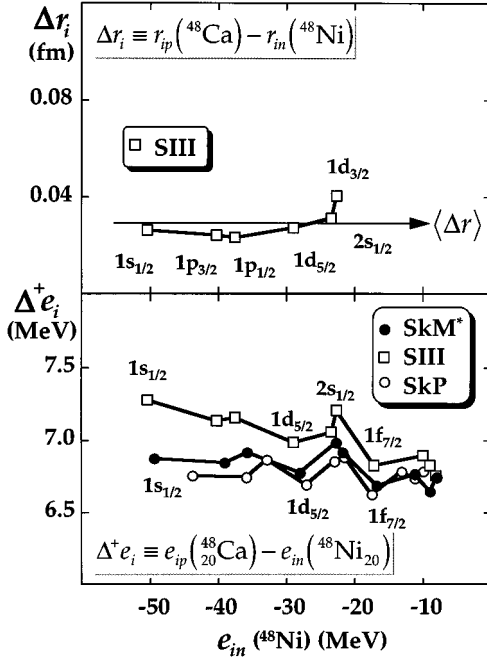


FIG. 11. Bottom: Difference  $\Delta^+ e_i [i \equiv (n\ell j)]$  between the proton single-particle energies in  $^{48}\text{Ca}$  and the neutron single-particle energies in  $^{48}\text{Ni}$ , calculated in the HF+SkM $^*$ , HF+SkP, and HF+SIII models. Top: Difference  $\Delta r_i$  between the rms radii of proton states in  $^{48}\text{Ca}$  and the rms radii of neutron states in  $^{48}\text{Ni}$ , calculated in the HF+SIII model. The average value  $\langle \Delta r \rangle \equiv \sqrt{\langle r_p^2 \rangle \times \langle^{48}\text{Ca}\rangle - \sqrt{\langle r_n^2 \rangle \langle^{48}\text{Ni}\rangle}}$  is indicated by the arrow.

bound orbits (such as  $1f_{7/2}$ ), the value of  $\Delta r_i$  can be as large as 0.11 fm. The results presented in Figs. 10 and 11 indicate that the Thomas-Ehrman effect is significant in medium-mass proton-rich nuclei. In particular, it explains the dependence of  $\Delta^- e_i$  and  $\Delta^+ e_i$  on the separation energy, and it can lead to the modification of transition rates in drip-line systems.

## VII. DIPROTON DECAY OF $^{48}\text{Ni}$

The diproton decay lifetime of  $^{48}\text{Ni}$  has been estimated using the Wentzel-Kramers-Brillouin (WKB) expression for the partial width:

$$\Gamma_{2p} = \theta^2 \mathcal{N} \frac{\hbar^2}{4\mu} \exp \left[ -2 \int_{r_{\text{in}}}^{r_{\text{out}}} dr k(r) \right], \quad (12)$$

where  $\theta^2$  is the spectroscopic factor for finding a diproton in the correlated  $L=0$  state,  $\mu$  is the reduced mass,  $r_{\text{in}}$  and  $r_{\text{out}}$  are the classical inner and outer turning points, respectively,  $\mathcal{N}$  is the normalization factor,

$$\mathcal{N} \int_0^{r_{\text{in}}} dr \frac{1}{k(r)} \cos^2 \left[ \int_0^r dr' k(r') - \frac{\pi}{4} \right] = 1, \quad (13)$$

and  $k(r)$  is the wave number given by

$$k(r) = \sqrt{\frac{2\mu}{\hbar^2} |Q_{2p} - V_{2p}(r)|}. \quad (14)$$

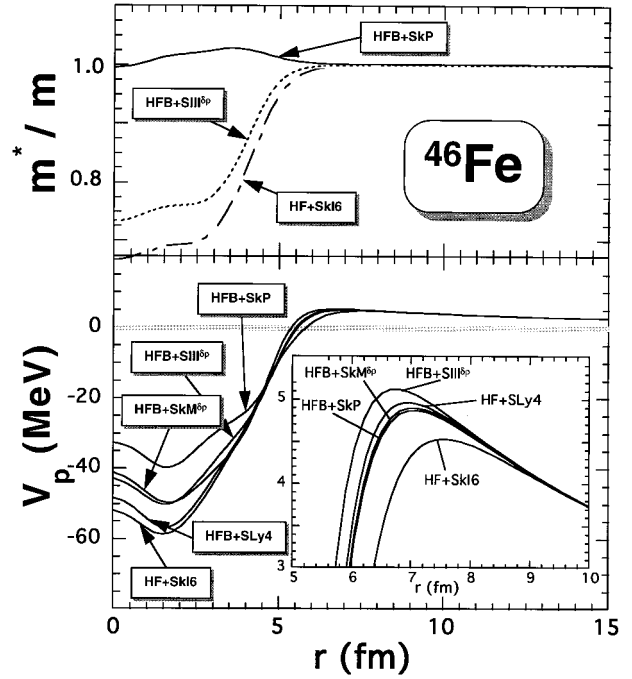


FIG. 12. Bottom: self-consistent proton potential  $V_p$  in  $^{46}\text{Fe}$  obtained in the HF and HFB calculations with different effective interactions. The details of  $V_p$  in the region of the Coulomb barrier are magnified in the inset. Top: proton effective mass  $m^*/m$  in the HFB+SkP, HFB+SIII $^{\delta\rho}$ , and HF+SkI6 models.

In Eq. (14),  $Q_{2p} = -S_{2p} > 0$ , and  $V_{2p}(r)$  is the average diproton potential (including the Coulomb potential). In our calculations,  $V_{2p}$  has been approximated by  $2V_p(r)$ , where  $V_p(r)$  is the self-consistent proton potential for  $^{46}\text{Fe}$ . Figure 12 (bottom) displays the calculated proton potentials for  $^{46}\text{Fe}$  in HF, HFB, and RMF approaches with different effective interactions. The average potentials differ both in the nuclear interior and in the Coulomb barrier region (see inset). The main origin of the differences inside the nucleus is the proton effective mass  $m^*/m$  which, for most interactions employed in our study, is significantly lower than the one inside the nuclear volume (see Sec. III). The upper portion of Fig. 12 illustrates the behavior of  $m^*/m$  for HFB+SkP, HFB+SkM $^{\delta\rho}$ , and HF+SkI6. (Results for SLy4 are very similar to those for SkI6.) Generally, the reduced effective mass gives rise to a deeper single-particle potential. Indeed, the proton potential in HFB+SkM $^{\delta\rho}$  (or HF+SkI6) is approximately 25% (or 50%) deeper than that in HFB+SkP. To take into account the effect of the effective mass, the WKB relation (14) has to be modified. The resulting wave number is given by

$$k(r) = \sqrt{\frac{2\mu}{\hbar^2} \frac{m^*(r)}{m} |Q_{2p} - V_{2p}(r)|}. \quad (15)$$

In the barrier region, SkM $^{\delta\rho}$ , Sly4, and SkP models give rather similar proton potentials. The SkI6 parametrization yields a slightly lower Coulomb barrier (by  $\sim 400$  keV) and significantly larger barrier radius  $r_B$ . The highest barrier and the lowest value of  $r_B$  are predicted by SIII $^{\delta\rho}$ .

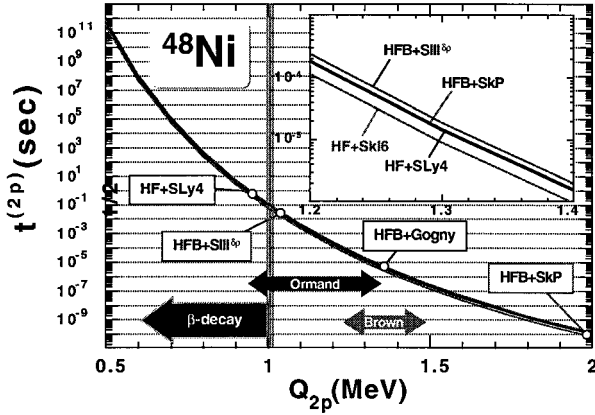


FIG. 13. Diproton partial decay half-lives for  $^{48}\text{Ni}$  predicted in the HFB+SkP, HFB+SIII $^{\delta p}$ , HF+SkI6, and HF+SLy4 models as a function of  $Q_{2p}$ . All theoretical results lie in a narrow band (detailed behavior in the region  $1.2 \leq Q_{2p} < 1.4$  MeV is shown in the inset). The  $Q_{2p}$  values predicted by different models are indicated by open circles, and those by Brown [4] and Ormand [6] by arrows. (For the corresponding values of  $Q_{2p} = -S_{2p}$ , see Table III.)

In order to check the sensitivity of the predicted half-lives to the details of the proton mean field, calculations were performed for different self-consistent potentials. For the spectroscopic factor we adopted the value of  $\theta^2 = 0.55/4 = 0.1375$  from Brown [4]. The diproton partial decay half-lives for  $^{48}\text{Ni}$ ,  $t_{1/2}^{(2p)} = \hbar \ln 2 / \Gamma_{2p}$ , are shown in Fig. 13 for the HFB+SkP, HFB+SIII $^{\delta p}$ , HF+SkI6, and HF+SLy4 models. It is seen that all theoretical results cluster in a rather narrow band. To see the differences between the models, the region  $1.2 \text{ MeV} \leq Q_{2p} < 1.4 \text{ MeV}$  has been magnified in the insert. For the models that predict the most different proton potentials, i.e., HFB+SIII $^{\delta p}$  and HF+SkI6, calculated half-lives differ by only a factor of 2. One can thus conclude that the values of  $t_{1/2}^{(2p)}$  are not, at least in this mass region, sensitive to the details of the nuclear mean field. The effect on  $t_{1/2}^{(2p)}$  due to changes in  $V_{2p}$  seems to be less important than other theoretical uncertainties, related, e.g., to the estimate of  $\theta^2$  or  $Q_{2p}$ .

As seen in Fig. 13, the main factor in determining  $t_{1/2}^{(2p)}$  is  $Q_{2p}$ . Indeed, in the energy range of  $0.5 \leq Q_{2p} < 2.0$  MeV, the diproton half-lives vary by more than 22 orders in magnitude; that is, the energy window for the experimental observation of diproton emitters is extremely narrow. The  $Q_{2p}$  values obtained in different models are indicated by open circles in Fig. 13. Predictions by Brown [4] and Ormand [6] (including error bars) are shown by arrows. (Lifetime predictions for other models can be obtained by using  $S_{2p}$  values from Table III.) Based on phenomenological studies supported by shell-model analyses (Brown and Ormand), one can conclude that  $t_{1/2}^{(2p)}$  for  $^{48}\text{Ni}$  is between  $10^{-7}$  and 1 s. This is consistent with the  $S_{2p}$  values given by ETFSI, HFB+SIII $^{\delta p}$ , HFB+Gogny, HF+SLy4, and RMF+PL40. The theoretical uncertainty in  $S_{2p}$  is dramatically amplified for  $t_{1/2}^{(2p)}$ . For instance, a difference in  $S_{2p}$  of about 500 keV between HF+SIII and HF+SIII $^{\delta p}$  gives rise to the difference of nearly 13 orders of magnitude in  $t_{1/2}^{(2p)}$ . Given the predicted  $\beta$ -decay half-life of  $^{48}\text{Ni}$ , 9.2 ms [4], the value of

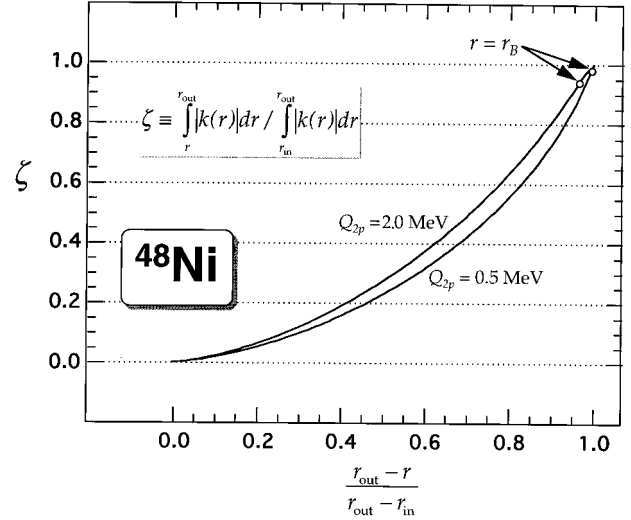


FIG. 14. Normalized contribution to the WKB exponent, Eq. (16), as a function of the relative distance from the outer turning point,  $(r_{\text{out}} - r)/(r_{\text{out}} - r_{\text{in}})$  for  $Q_{2p} = 0.5$  and  $2.0$  MeV in  $^{48}\text{Ni}$ . The curves are representative of all models displayed in Fig. 12. The open circles indicate the distance corresponding to the Coulomb barrier radius  $r_B$ .

$Q_{2p}$  should be larger than 1 MeV to enable experimental observation of diproton emission from this nucleus (see Fig. 13).

To understand the weak sensitivity of  $t_{1/2}^{(2p)}$  to the details of  $V_{2p}$ , Fig. 14 displays the (normalized) contribution to the exponent appearing in Eq. (12) from different regions in the barrier,

$$\zeta(r) \equiv \frac{\int_r^{r_{\text{out}}} dr k(r)}{\int_{r_{\text{in}}}^{r_{\text{out}}} dr k(r)}, \quad (16)$$

as a function of the relative distance from the outer turning point. By construction,  $\zeta(r_{\text{out}} = 2Ze^2/Q_{2p}) = 0$  and  $\zeta(r_{\text{in}}) = 1$ . The calculations are performed for  $Q_{2p} = 0.5$  and  $2.0$  MeV, thus covering the whole energy window of Fig. 13. It has been checked that the curves presented in Fig. 14 are very similar in all of the models employed in our study. The points corresponding to the barrier radius  $r_B$  are indicated by open circles. It is seen that more than 94–99 % of the exponent Eq. (16) comes from the region  $r > r_B$ , which is almost solely determined by the pure Coulomb interaction  $V_C = 2Ze^2/r$ . This result demonstrates that  $t_{1/2}^{(2p)}$  can be well estimated by ignoring the details of the proton potential, as was done in previous estimates [4,6] based on the  $R$ -matrix theory.

## VIII. CONCLUSIONS

Several models based on the self-consistent mean-field approach were applied to proton-rich nuclei from the proton-rich  $sdf$  region. The overall agreement with experimental

data and shell-model calculations for  $S_{2p}$  in the  $sdf$  region is satisfactory. In particular, the mean-field calculations systematically predict the two-proton drip line to lie between  $^{42}\text{Cr}$  and  $^{44}\text{Cr}$ ,  $^{44}\text{Fe}$  and  $^{46}\text{Fe}$ , and  $^{48}\text{Ni}$  and  $^{50}\text{Ni}$ . This result gives us some confidence in extrapolating the results of our mean-field calculations towards the neutron drip line where shell-model calculations are not feasible.

Self-consistent Coulomb energies, taking into account the Thomas-Ehrman shift, allowed us to estimate the single-particle levels around the unbound doubly magic nucleus  $^{48}\text{Ni}$ . As a by-product of our analysis, another doubly magic, neutron-rich system,  $^{70}\text{Ca}_{50}$ , was calculated to lie on the border of two-neutron stability.

According to our study, diproton emission half-lives depend mainly on the two-proton separation energy and very weakly on the intrinsic structure of diproton emitters. The very weak dependence of  $t_{1/2}^{(2p)}$  on the details of the proton potential demonstrated in this study justifies the simple estimates of Refs. [4,6] based on the  $R$ -matrix theory.

## ACKNOWLEDGMENTS

Useful discussions with W. Walters and W. E. Ormand are gratefully acknowledged. Oak Ridge National Laboratory is managed for the U.S. Department of Energy by Lockheed Martin Energy Systems, Inc. under Contract No. DE-AC05-84OR21400. The Joint Institute for Heavy Ion Research has as member institutions the University of Tennessee, Vanderbilt University, and the Oak Ridge National Laboratory; it is supported by the members and by the Department of Energy through Contract No. DE-FG05-87ER40361 with the University of Tennessee. Theoretical nuclear physics research is supported by the U.S. Department of Energy through Contract No. DE-FG05-93ER40770 (University of Tennessee) and through Contract No. DE-FG05-87ER40376 (Vanderbilt University). This research was supported in part by the Polish Committee for Scientific Research under Contract No. 2 P03B 034 08, by the GSI (Darmstadt), and by the German BMFT.

- 
- [1] C.N. Davids, P.J. Woods, J.C. Batchelder, C.R. Bingham, D.J. Blumenthal, L.T. Brown, B.C. Busse, L.F. Conticchio, T. Davidson, S.J. Freeman, M. Freer, D.J. Henderson, R.J. Irvine, R.D. Page, H.T. Penttilä, A.V. Ramayya, D. Seweryniak, K.S. Toth, W.B. Walters, A.H. Wuosmaa, and B.E. Zimmerman, in Proceedings of the International Conference on Exotic Nuclei and Atomic Masses, Arles, France, 1995; Phys. Rev. Lett. (to be published).
- [2] S. Hofmann, in *Particle Emission from Nuclei*, edited by M. Ivascu and D.N. Poenaru (CRC, Boca Raton, 1989), Vol. 2, Chap. 2; in *Handbook on Nuclear Decay Modes*, edited by D. Poenaru and W. Greiner (Oxford University Press, New York, 1995).
- [3] A. Mueller and B. Sherril, Annu. Rev. Nucl. Part. Sci. **43**, 529 (1993).
- [4] B.A. Brown, Phys. Rev. C **43**, R1513 (1991); **44**, 924 (E) (1991).
- [5] E. Caurier, A.P. Zuker, A. Poves, and G. Martínez-Pinedo, Phys. Rev. C **50**, 225 (1994).
- [6] W.E. Ormand, Phys. Rev. C (to be published).
- [7] U. Fano, Phys. Rev. **124**, 1866 (1961).
- [8] B. Blank, S. Andriamonje, R. Del Moral, J.P. Dufour, A. Fleury, Th. Josso, M.S. Pravikoff, S. Czajkowski, Z. Janas, A. Piechaczek, E. Roeckl, K.-H. Schmidt, K. Sümmerer, W. Trinder, M. Weber, T. Brohm, A. Grewe, E. Hanelt, A. Heinz, A. Junghans, C. Röhl, S. Steinhäuser, B. Voss, and M. Pfützner, Phys. Rev. C **50**, 2398 (1994).
- [9] C. Détraz, R. Anne, P. Bricault, D. Guillemaud-Mueller, M. Lewitowicz, A.C. Mueller, Y.H. Zhang, V. Borrel, J.C. Jacmart, F. Pougheon, A. Richard, D. Bazin, J.P. Dufour, A. Fleury, F. Hubert, and M.S. Pravikoff, Nucl. Phys. **A519**, 529 (1990).
- [10] V. Borrel, R. Anne, D. Bazin, C. Borcea, G.G. Chubarian, R. Del Moral, C. Détraz, S. Dogny, J.P. Dufour, L. Faux, A. Fleury, L.K. Fifield, D. Guillemaud-Mueller, F. Hubert, E. Kashy, M. Lewitowicz, C. Marchand, A.C. Mueller, F. Pougheon, M.S. Pravikoff, M.G. Saint-Laurent, and O. Sorlin, Z. Phys. A **344**, 135 (1992).
- [11] D. Guillemaud-Mueller, J.C. Jacmart, E. Kashy, A. Latimier, A.C. Mueller, F. Pougheon, A. Richard, Yu.E. Penionzhkevich, A.G. Artukh, A.V. Belozorov, S.M. Lukyanov, R. Anne, P. Bricault, C. Detraz, M. Lewitowicz, Y. Zhang, Yu.S. Lyutostansky, M.V. Zverev, D. Bazin, and W.D. Schmidt-Ott, Phys. Rev. C **41**, 937 (1990).
- [12] D. Guillemaud-Mueller, Yu.E. Penionzhkevich, R. Anne, A.G. Artukh, D. Bazin, V. Borrel, C. Detraz, D. Guerreau, B.A. Gvozdev, J.C. Jacmart, D.X. Jiang, A.M. Kalinin, V.V. Kamanin, V.B. Kutner, M. Lewitowicz, S.M. Lukyanov, A.C. Mueller, Nguyen Hoai Chau, F. Pougheon, A. Richard, M.G. Saint-Laurent, and W.D. Schmidt-Ott, Report No. JINR-E7-88-650, 1988.
- [13] M. Lewitowicz, Yu.E. Penionzhkevich, A.G. Artyukh, A.V. Belozorov, S.M. Lukyanov, D. Guillemaud-Mueller, Zh.K. Zhakmar, E. Kashy, A. Latimer, A.K. Mueller, F. Pougheon, A. Richard, R. Anne, P. Bricault, C. Detraz, I. Zhong, D. Bazin, W.D. Schmidt-Ott, in Proceedings of the Annual Conference on Nuclear Spectroscopy and the Structure of Atomic Nuclei, Leningrad, 1990, p. 50.
- [14] X.L. Tu, X.G. Zhou, D.J. Vieira, J.M. Wouters, Z.Y. Zhou, H.L. Seifert, and V.G. Lind, Z. Phys. A **337**, 361 (1990).
- [15] M. Weber, C. Donzaud, J.P. Dufour, H. Geissel, A. Grewe, D. Guillemaud-Mueller, H. Keller, M. Lewitowicz, A. Magel, A.C. Mueller, G. Munzenberg, F. Nickel, M. Pfützner, A. Piechaczek, M. Pravikoff, E. Roeckl, K. Rykaczewski, M.G. Saint-Laurent, I. Schall, C. Stephan, K. Sümmerer, L. Tassan-Got, D.J. Vieira, and B. Voss, Z. Phys. A **343**, 67 (1992).
- [16] M. Bernas, P. Armbruster, S. Czajkowski, H. Faust, J.P. Bocquet, and R. Brissot, Phys. Rev. Lett. **67**, 3661 (1991).
- [17] Ch. Engelmann, F. Ameil, P. Armbruster, M. Bernas, S. Czajkowski, Ph. Dessagne, C. Donzaud, H. Geissel, A. Heinz, Z. Janas, C. Kozhuharov, Ch. Miehé, G. Münzenberg, M. Pfützner, C. Röhl, W. Schwab, C. Stéphan, K. Sümmerer, L. Tassan-Got, and B. Voss, Z. Phys. A **352**, 351 (1995).
- [18] M. Girod, Ph. Dessagne, M. Bernas, M. Langevin, F. Pougheon, and P. Roussel, Phys. Rev. C **37**, 2600 (1988).

- [19] K.-L. Kratz, B. Pfeiffer, A. Woehr, and P. Möller, *Z. Phys. A* **332**, 419 (1989).
- [20] S. Kamenetzkiy, J. Speth, G. Tertychnyi, and J. Wambach, *Z. Phys. A* **346**, 253 (1993).
- [21] Z. Szymański and J. Żylicz, in *Nuclear Physics of Our Times*, edited by V.A. Ramayya (World Scientific, Singapore, 1993), p. 100.
- [22] V.I. Goldansky, *Nucl. Phys.* **19**, 482 (1960).
- [23] J. Dobaczewski, H. Flocard, and J. Treiner, *Nucl. Phys. A* **422**, 103 (1984).
- [24] R. Smolańczuk and J. Dobaczewski, *Phys. Rev. C* **48**, R2166 (1993).
- [25] P. Möller, J.R. Nix, W.D. Myers, and W.J. Swiatecki, *At. Data Nucl. Data Tables* **59**, 185 (1995).
- [26] R. Bengtsson, P. Möller, J.R. Nix, and J.-Y. Zhang, *Phys. Scr.* **29**, 402 (1984).
- [27] H. Toki, Y. Sugahara, D. Hirata, B.V. Carlson, and I. Tanihata, *Nucl. Phys.* **A524**, 633 (1991).
- [28] K.-L. Kratz, Report No. IKMz 94-3, 1994 [*Nuclei in the Cosmos*, Proceedings of the 3rd International Symposium on Nuclear Astrophysics, Gran Sasso, Italy, 1994 (to be published)].
- [29] F. Pougheon, J.C. Jamart, E. Quiniou, R. Anne, D. Bazin, V. Borrel, J. Galin, D. Guerreau, D. Guillemaud-Mueller, A.C. Mueller, E. Roeckl, M.G. Saint-Laurent, and C. Détraz, *Z. Phys. A* **327**, 17 (1987).
- [30] L. Faux, M.S. Pravikoff, S. Andriamonje, B. Blank, R. Del Moral, J.-P. Dufour, A. Fleury, C. Marchand, K.-H. Schmidt, K. Sümmerer, T. Brohm, H.-G. Clerc, A. Grewe, E. Hanelt, B. Voss, and C. Ziegler, *Phys. Rev. C* **49**, 2440 (1994).
- [31] E.P. Wigner, in *Proceedings of the Robert Welch Foundation Conference on Chemical Research*, edited by W.O. Milligan (The Robert A. Welch Foundation, Houston, 1958), Vol. I, p. 86.
- [32] W. Benenson, *Nukleonika* **20**, 775 (1975).
- [33] W. Benenson and E. Kashy, *Rev. Mod. Phys.* **51**, 527 (1979).
- [34] M.S. Antony and A. Pape, *Phys. Rev. C* **30**, 1286 (1984).
- [35] I.V. Poplavskii, *Phys. At. Nucl.* **57**, 600 (1994).
- [36] W.E. Ormand and B.A. Brown, *Nucl. Phys.* **491**, 1 (1989).
- [37] J. Dobaczewski, W. Nazarewicz, and T.R. Werner, *Phys. Scr.* **T56**, 15 (1995).
- [38] R.R. Chasman, *Phys. Rev. C* **14**, 1935 (1976).
- [39] V.E. Starodubsky and M.V. Zverev, *Phys. Lett. B* **276**, 269 (1992).
- [40] N. Tajima, P. Bonche, H. Flocard, P.-H. Heenen, and M.S. Weiss, *Nucl. Phys.* **A551**, 434 (1993).
- [41] M. Beiner, H. Flocard, N. Van Giai, and P. Quentin, *Nucl. Phys.* **A238**, 29 (1975).
- [42] J. Bartel, P. Quentin, M. Brack, C. Guet, and H.B. Håkansson, *Nucl. Phys.* **A386**, 79 (1982).
- [43] S.T. Belyaev, A.V. Smirnov, S.V. Tolokonnikov, and S.A. Fayans, *Sov. J. Nucl. Phys.* **45**, 783 (1987).
- [44] J. Dobaczewski, W. Nazarewicz, T.R. Werner, J.-F. Berger, C.R. Chinn, and J. Dechargé, *Phys. Rev. C* (to be submitted).
- [45] J. Dechargé and D. Gogny, *Phys. Rev. C* **21**, 1568 (1980).
- [46] J.F. Berger, M. Girod, and D. Gogny, *Nucl. Phys.* **A502**, 85c (1989).
- [47] J.-F. Berger, M. Girod, and D. Gogny, *Comput. Phys. Commun.* **63**, 395 (1991).
- [48] P.-G. Reinhard, in *Computational Nuclear Physics I*, edited by K. Langanke, J.A. Maruhn, and S.E. Koonin (Springer-Verlag, Berlin, 1990), p. 28.
- [49] P.-G. Reinhard and H. Flocard, *Nucl. Phys.* **A584**, 467 (1995).
- [50] E. Chabanat, P. Bonche, P. Haensel, J. Meyer, and F. Schaeffer, *Phys. Scr.* **T56**, 231 (1995).
- [51] M.M. Sharma, M.A. Nagarajan, and P. Ring, *Phys. Lett. B* **312**, 377 (1993).
- [52] C. Greiner and P.-G. Reinhard, *Z. Phys. A* **342**, 379 (1992).
- [53] M. Rufa, J.A. Maruhn, W. Greiner, P.-G. Reinhard, and J. Friedrich, *Z. Phys. A* **323**, 323 (1986).
- [54] W. Nazarewicz, J. Dobaczewski, and T.R. Werner, *Phys. Scr.* **T56**, 9 (1995).
- [55] J. Dobaczewski, I. Hamamoto, W. Nazarewicz, and J.A. Sheikh, *Phys. Rev. Lett.* **72**, 981 (1994).
- [56] J. Dobaczewski, W. Nazarewicz, and T.R. Werner, *Z. Phys.* (in press).
- [57] Y. Aboussir, J.M. Pearson, A.K. Dutta, and F. Tondeur, *Nucl. Phys.* **A549**, 155 (1992); J.M. Pearson (private communication).
- [58] A.S. Umar, M.R. Strayer, J.-S. Wu, D.J. Dean, and M.C. Güçlü, *Phys. Rev. C* **44**, 2512 (1991).
- [59] J. Dobaczewski and W. Nazarewicz, *Phys. Rev. C* **51**, R1070 (1995).
- [60] G. Audi and A.H. Wapstra, *Nucl. Phys.* **A565**, 1 (1993); **A565**, 66 (1993).
- [61] N. Auerbach, J. Hüfner, A.K. Kerman, and C.M. Shakin, *Rev. Mod. Phys.* **44**, 48 (1972).
- [62] S. Schlomo, *Rep. Prog. Phys.* **41**, 957 (1978).
- [63] N. Van Giai, D. Vautherin, M. Veneroni, and D.M. Brink, *Phys. Lett.* **35B**, 135 (1971).
- [64] R.G. Thomas, *Phys. Rev.* **81**, 148 (1951); **88**, 1109 (1952).
- [65] J.B. Ehrman, *Phys. Rev.* **81**, 412 (1951).
- [66] A. Bohr and B.R. Mottelson, *Nuclear Structure* (W.A. Benjamin, New York, 1969), Vol 1.